optica

Tailoring the potential landscape of room-temperature single-mode whispering gallery polariton condensate

Hyun Gyu Song, Sunghan Choi, Chung Hyun Park, Su-Hyun Gong, Chulwon Lee, Min Sik Kwon, Dae Gwang Choi, Kie Young Woo, and Yong-Hoon Cho*

Department of Physics and KI for the NanoCentury, Korea Advanced Institute of Science and Technology (KAIST), 291 Daehak-ro, Yuseong-gu, Daejeon 34141, South Korea
*Corresponding author: yhc@kaist.ac.kr

A key point of exciton polaritons is real-time controllability of potential energy and its landscape due to the hybrid nature of excitons and photons. Although wide-bandgap semiconductors allow us to generate room-temperature polaritons, unintentional localizations of two-dimensional cavities caused by disorder (dephasing and potential fluctuation) still hinder the establishment of ballistic extensions of polariton condensates. This ballistic extension accompanies spatial coherence, an essential factor for phase transitions as well as any quantum controls. Here we propose a room-temperature polariton system with ultralow disorder capable of one-dimensional ballistic propagation. Selectively grown GaN wire dramatically reduces disorder in both the exciton perspective via dislocation bending and the photon perspective through crystallographically defined hexagonal cavities. This high-quality wire on a substrate forms triangular whispering gallery modes and allows us to demonstrate the room-temperature single-mode one-dimensional polariton condensate with ballistic propagation. This ballistic propagation is manipulated by active real-time control of the potential gradient. The correlation between propagation distances deduced from real and momentum space provides strong evidence of ballistic propagations in an ultralow-disordered one-dimensional system. © 2019 Optical Society of America under the terms of the OSA Open Access Publishing Agreement

https://doi.org/10.1364/OPTICA.6.001313

1. INTRODUCTION

Semiconductor microcavities can allow us to enter the hybrid nature of exciton cavity polaritons (polaritons) [1], which comply with Bose–Einstein statistics [2,3]. A crucial benefit of the polariton system is real-time controllability of polariton potential via optical manipulation [4,5] or acoustic waves [6]. This potential engineering can make challenging photonic devices feasible, such as polariton spin switches [7], transistors [8], phase modulators [9], and resonant tunneling diodes [10]. The potential engineering can be conducted by the manipulation of two variables, polariton potential energy and potential landscape [11–14]. Remarkably, this potential landscape can yield ballistic extension in the polariton condensate, which accompanies the robust coherence of the polariton condensate due to spatial decoupling [12,15] between polaritons and the exciton reservoir. This macroscopic quantum coherence is an essential factor for phase transition research, such as the Berezinskii–Kosterlitz–Thouless phase transition [15] and quantum vortex [16], as well as the next generation of the polaritonic quantum fluid circuit.

Since semiconductor cavities with ultralow disorder are essential for the control of the polariton potential landscape, state-of-the-art two-dimensional cavities based on III-arsenide materials have been mainly used, even though cryogenic temperatures are required. In order to overcome the temperature limitation, wide-bandgap semiconductors, such as perovskites, ZnO, and III-nitride systems, are promising candidates for generating room-temperature polaritons due to their large exciton (X) binding energy and high oscillator strength. In the case of perovskite materials, this ballistic transport of polariton condensate with high velocity was recently reported in a dielectric distributed Bragg reflector (DBR) based on a one-dimensional structure at room temperature [17]. Also, a one-dimensional system based on ZnO obtains the temporal and spatial information of the ballistic transports for multimode polaritons [18]. However, fabrication of a III-nitride-based planar microcavity for high-quality DBR is still challenging due to the low refractive index contrast and the large lattice misfit between AlN and GaN. Nevertheless, a conventional two-dimensional room temperature polariton condensate based on III-nitride semiconductors was previously reported using diverse structures, such as bulk [19] or multiple quantum wells [20,21] in a hybrid DBR as well as nanowires [22,23] or a membrane [24,25] embedded in an oxide-based DBR. These two-dimensional microcavity systems still confronted unintentional localizations [19–25] in the lateral direction

blurring out the potential landscape. These unintentional localizations are caused by both the excitonic disorder from dislocations due to lattice mismatch and the photonic disorder from the imperfection of fabrication. On the other hand, one-dimensional structures (i.e., wire structures) with high-quality X and cavity photons (CPs), analogous to Tonks–Girardeau gas [26,27] in a one-dimensional ultracold atom, are unexplored systems for potential landscape manipulation, for which we can expect enhanced directionality as a result of the reduced dimensionality [28].

Here, we propose a single-mode, triangular whispering gallery (tri-WG) polariton condensate in a GaN hexagonal wire on a substrate as the room-temperature polariton platform with ultralow disorder for optically tailoring the polariton potential landscape. Excitonic disorder can be free from dephasing because of dislocation bending [29] to the bottom part of the surface and strain relaxation [30] along the c axis. Moreover, photonic disorder is dramatically reduced due to the crystallographically defined hexagonal facets, which generate the spontaneous formation of triangular whispering gallery modes (tri-WGMs) without any fabrication. The tri-WGMs can robustly keep the quality factor (Q factor) and CP energy from being influenced by disorder due to a lower number of reflection faces and greater distance from the edges. Thus, tri-WG polaritons resulting from the strong coupling between three-dimensional X and one-dimensional tri-WG photons in the wire can be generated in the paved potential system with ultralow disorder. We first demonstrate the one-dimensional ballistic propagation of the single-mode tri-WG polariton condensate at room temperature. This ballistic propagation can be manipulated by active control of the potential gradient and form the state by spatially decoupling from the exciton reservoir. The good consistency between characterizations of propagation deduced from real and momentum space provides strong evidence of ballistic propagations due to an ultralow-disordered one-dimensional system.

2. METHOD

A. Coupled Oscillator Hamiltonian

To calculate our results, we use a coupled oscillator Hamiltonian,

$$\begin{pmatrix} E_{ph}(\theta) & \hbar\Omega_1/2 & \hbar\Omega_2/2 \\ \hbar\Omega_1/2 & X_i & 0 \\ \hbar\Omega_2/2 & 0 & X_j \end{pmatrix} \begin{pmatrix} \alpha \\ \beta \\ \gamma \end{pmatrix} = E_{pol}(\theta) \begin{pmatrix} \alpha \\ \beta \\ \gamma \end{pmatrix}.$$

Here, Ω_1 and Ω_2 are the Rabi splitting frequencies for exciton energies X_i and X_j ($X_i = X_A$, $X_j = X_B$ for TE and $X_i = X_B, X_j = X_C$ for TM, respectively). For rapid calculation, we use a plane-wave model to estimate tri-WGMs inside the wire. Here, $E_{ph}(\theta) = \frac{E_0}{\sqrt{(1-\frac{\sin^2\theta}{n^2})}}$ is the photonic dispersion of the tri-WGM, $E_0 = (\frac{2hc}{9nR})[N + \frac{3}{\pi}\arctan(\beta\sqrt{3n^2-4})]$ is the ground CP energy of the tri-WGM, where n is the refractive index of the cavity (uniaxial birefringent index n_o and n_e for TE and TM, respectively), N is the photonic mode number, R is the radius of a hexagonal cavity, h the Planck constant, and c is the speed of light. The factor β is equal to n and $1/n$ for TE and TM modes, respectively. We assumed $\hbar\Omega_{Rabi}$ is independent of positions due to the negligible variation of the spatial overlap between photons and excitons for the micro-sized diameters. The parameters we used in the calculation correspond to

$X_A = 3.429$ eV, $X_B = 3.434$ eV, $X_C = 3.450$ eV, $n_0 = 3.013$, $n_e = 3.020$, and $R = 830$ nm.

B. Tail Fitting of an Airy Function

To consider the disorder effect via the correlation between real space and momentum space, we use the Gross–Pitaevskii equation for the polariton condensate as follows:

$$i\hbar\frac{\partial\psi(r)}{\partial t} = \left\{E_0 - \frac{\hbar^2}{2m}\nabla_r^2 + \hbar g|\psi(r)|^2 + \hbar g_X n_R(r) \right.$$
$$\left. + \frac{i\hbar}{2}[R[n_R(r)] - \gamma_p] + V_{dis}(r)\right\}\psi(r).$$

Here, E_0 is the minimum energy of the lower polariton branch, m is the effective mass of the polaritons, g is the polariton–polariton interaction coefficient, g_X is the polariton–reservoir interaction coefficient, and γ_p is the polariton loss rate, which is the inverse of the polariton lifetime.

To consider the disorder effect via the correlation between real space and momentum space, we use the regime far outside the pump area devised by Wouters et al. [31]. In this region, the density of the polariton condensate is too small to feel the repulsive interaction by the polaritons ($\hbar g|\psi(z)|^2 \sim 0$). Also, it is far from the pump area, so we can ignore the exciton reservoir related imaginary terms and polariton–reservoir interaction term ($\hbar g_X n_R(z) \sim 0$). V_{dis} is the disorder potential term, which is linear potential ($V_{dis} \sim \alpha z$) due to the slightly tapered geometry of our wire structure along the z axis. Here, it is worth noticing that the conventional method ($\partial^2 E/\partial k^2$) of extraction of the polariton effective mass approximation might be distorted due to the linear potential. Thus, we can simplify the Gross–Pitaevskii equation by considering our one-dimensional structure as follows:

$$\frac{\hbar^2}{2m}\frac{\partial^2}{\partial z^2}\psi(z) + \left\{\hbar(\omega_c - \omega_o) + \frac{i\hbar}{2\tau_p}\right\}\psi(z) + \alpha z\psi(z) = 0,$$

where τ_p corresponds to the polariton lifetime. Also, ω_c and ω_o are the energies of the finite momentum of the polariton state and ground state of polaritons, respectively. The corresponding solution can be expressed as

$$I = |\psi(z)|^2 = \left|c \times A_i\left(-\frac{k_c^2 + i\frac{k_c}{v_g\times\tau_p} + \frac{k_c^2}{\Delta E}\alpha z}{\left(-\frac{k_c^2}{\Delta E}\alpha z\right)^{\frac{2}{3}}}\right)\right|^2.$$

Here, ΔE and k_c are determined by measured angle-resolved photoluminescence, and α (~ 2.7 meV/μm) is extracted from the line scan data. The only fitting parameters are $v_g \times \tau_p$ and c. Thus, we can extract the decay length via tail fitting of the spatial profile [at the shaded area on the left and right sides in Fig. 5(b)]. If severe disorder exists, this simple modeling would not show very good agreement between real space and momentum space.

3. 1D MICROCAVITIES OF SELECTIVELY GROWN WIRES

Figure 1(a) depicts the selective area growth process of *undoped* GaN wires. A bird's-eye view of a scanning electron microscopy (SEM) image of the ensemble of GaN wires is shown in Fig. 1(b). Surprisingly, this growth method provides excellent regularity of the hexagonal shape, diameter, and height with low surface roughness, as seen in the SEM. For the photonic aspect, this method can ensure a regular hexagonal shape determined by the aspect
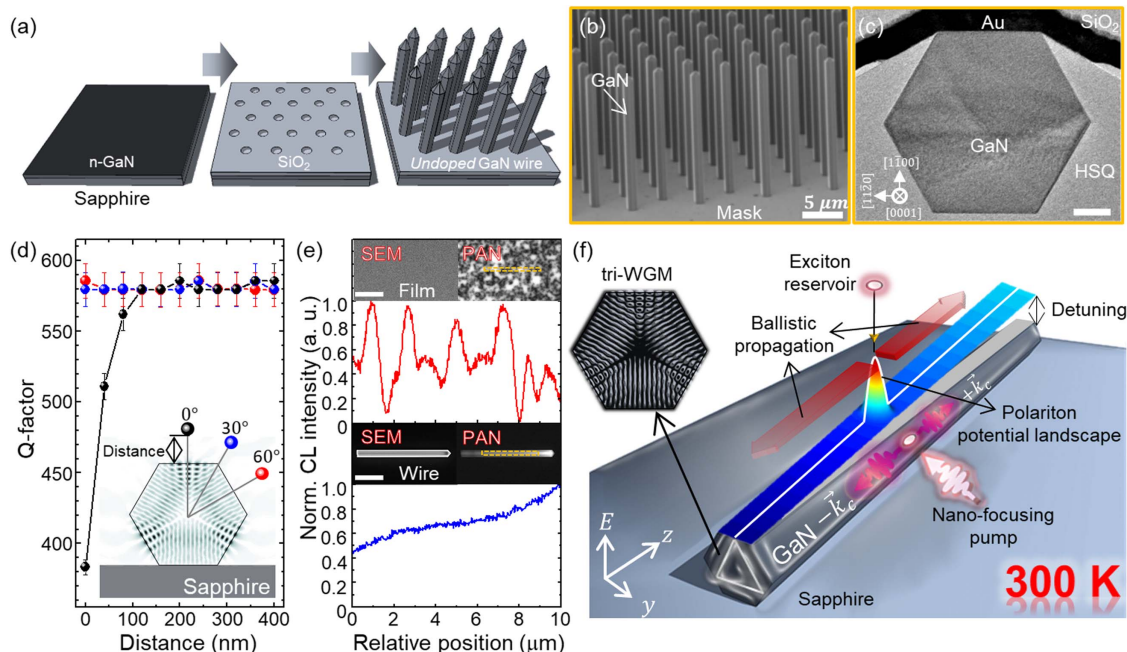
Fig. 1. GaN wire as a one-dimensional microcavity with tri-WGM. (a) Schematics of undoped GaN wires grown by selective area growth (b) a bird's-eye view SEM image of GaN wires, (c) HAADF-STEM image of a cross section of a single GaN wire. The scale bar indicates 200 nm. (d) FDTD simulation, showing the variation of the Q factor for the tri-WGM with the artificial link in relation to the distance between the wire surface and the link, (e) the spatial profile of the CL intensity of a conventional GaN film (top) and a high-quality single wire (bottom), (f) schematics of a tri-WG polariton with the potential landscape (white solid line) in real space (y, z) and energy (vertical axis).

ratio of the mask opening shape [32]. This regular hexagon can be crystallographically sustained along the c axis without any stacking faults so that the photonic energy fluctuation is negligible (± 0.69 meV; see Supplement 1). This six-fold rotation symmetry is crucial for the spontaneous generation of WGMs, as shown in the high-angle annular dark-field scanning transmission electron microscopy (HAADF-STEM) image for the cross section of the wire in Fig. 1(c). Only a tri-WGM [33] with an upward direction can dwell a long time, as shown in the inset of Fig. 1(d), due to leakage of the interface between the substrate and the wire. This tri-WGM can rigidly protect the Q factor and the resonance energy of the cavity from external influences because of the far distance of the electric fields from the edges and a lower number of reflection faces. To confirm this, we conducted a finite-difference time-domain (FDTD) simulation with variation of the distance of an artificial link (dust) with a 200 nm diameter, as shown in Fig. 1(d). We considered three directions, namely, 0° for the reflected surface, 30° for the edge, and 60° for the non-reflected surface. For 0°, the Q factor gradually decreased by as much as 64% and the CP energy showed a 3 meV redshift when the defect was attached to the reflected surface. Interestingly, there were no distinct effects on either the Q factor or the CP energy for 30° and 60° depending on the distance of the defect. This result indicates that tri-WGMs have stronger photonic tolerance than hexagonal WGMs, which is beneficial for the observation of robust polariton effects. For the excitonic aspect, the intensity fluctuation (i.e., dephasing) is dramatically suppressed by both dislocation bending [29] to the bottom part of the surface and the strain relaxation [30] along the c axis due to the lateral overgrowth mode. Consequently, most of the wire offers high-quality X, except for the bottom part acting as a sacrificial layer.

Figure 1(e) shows the characterization of cathodoluminescence (CL) for a GaN film (top) and a single GaN wire (bottom) dispersed on a silicon substrate. In the panchromatic CL image of the wire, there was no measurable dark spot compared to the film structure. The intensity fluctuation of the normalized profile for the wire (± 0.015) was more than one order smaller than the film (± 0.23). Therefore, this real one-dimensional cavity [34] with ultralow disorder yields robust room-temperature tri-WG polaritons capable of engineering the potential energy and landscape, as shown in Fig. 1(f).

4. ROOM-TEMPERATURE POLARITON CONDENSATE

To identify our one-dimensional cavity in the strong-coupling regime, we measured the angle-resolved micro-photoluminescence (ARPL) at room temperature. Figure 2(a) shows two different orientations of the polarization-resolved measurements. Electric fields of the TE modes (TM modes) is perpendicular (parallel) to the c axis. Figure 2(b) shows the polarization-resolved ARPL data obtained for detection angle θ_z for the TE (left side) and TM (right side) modes, respectively. Within given polarization, several lower polariton branches appeared, but upper polaritons were invisible due to absorption of the X continuum under the condition where Rabi splitting energy ($\hbar\Omega_{Rabi}$) was greater than X binding energy [35]. Multiple discrete states are revealed for detection angle θ_y due to two-dimensional optical confinement (see Supplement 1). Their dispersion aspects clearly indicate the strong coupling as follows. (i) The curvature of the higher-number modes (i.e., closer to the X energy) shows dispersion with lower curvature [36], while dispersions at lower energy have
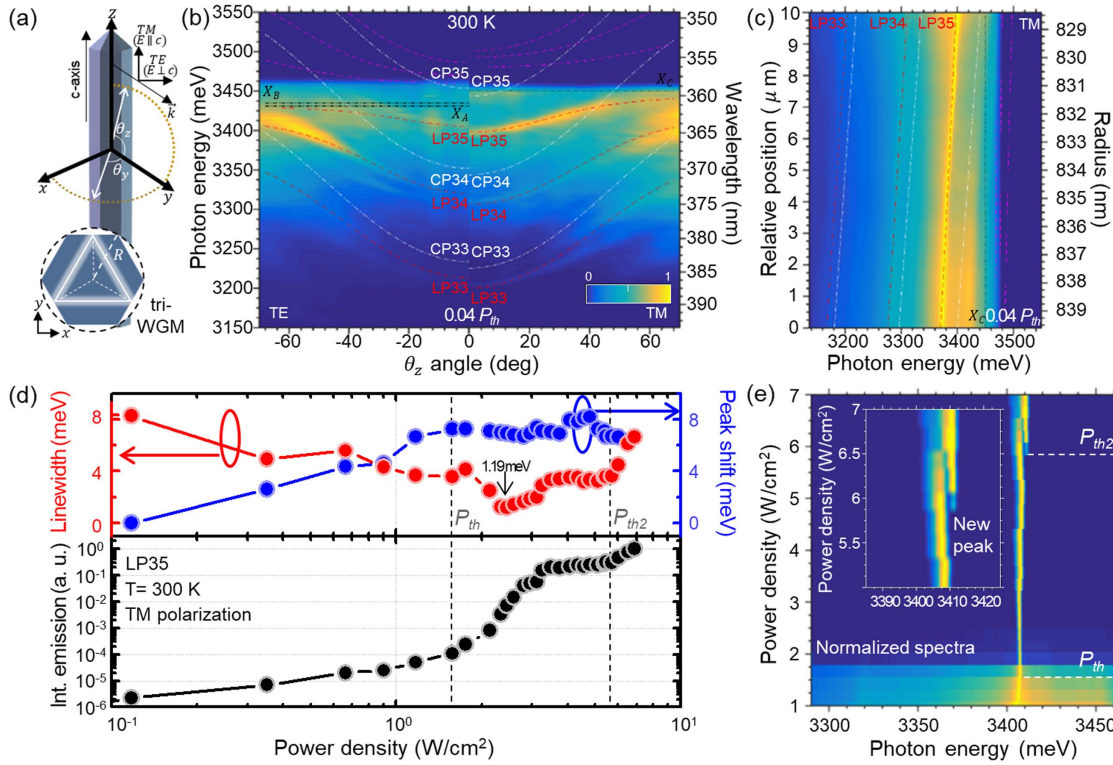
Fig. 2. Strong coupling and behavior of polariton condensate. (a) Schematic of polarizations and angles of the wire. (b) Polarization-resolved ARPL image on a linear scale. The green dashed-dotted lines show the A-exciton (X_A), B-exciton (X_B), and C-exciton (X_C). The white dashed-dotted lines and red dashed lines show calculated dispersions of pure tri-WGM cavity photons (CPs) in the weak-coupling regime and tri-WG lower polaritons (LPs) in the strong-coupling regime, respectively. (c) Position-dependent μPL image along the *c* axis for TM on a linear scale via excitation of 200 nm diameter, (d) variation of linewidth (top left) and peak shift (top right) with excitation power density for LP35; integrated PL intensity (bottom) from LP35 to the new peak, (e) normalized spectra in relation to pump power. Note the appearance of a new peak at the second threshold.

remarkably steeper curvature. (ii) The linewidth of higher-number modes is broader as the excitonic component increases (see Supplement 1) due to interaction with polaritons, phonons, and X. The polariton dispersion curve $[E_{\rm pol}(\theta)]$ was modeled by the coupled oscillator Hamiltonian [37] (see Method A in Section 2). The white dashed-dotted lines represent pure tri-WGMs in the weak-coupling regime, while the red dashed lines represent the calculated dispersion of TE- and TM-polarized tri-WG polaritons in the strong-coupling regime. The results regarding various calculated branches and their dispersion depending on polarizations are in excellent agreement with the measurements [Fig. 2(b)].

To investigate the cavity energy detuning effect, we characterized the position-dependent micro-photoluminescence (μPL) along the *c* axis of the same wire, as shown in Fig. 2(c). To calculate our results using the coupled oscillator Hamiltonian, we considered the variation of the radius along the *c* axis. The difference between the radius of the bottom and the top is 10 nm, confirmed by SEM. Here, the only fitting parameters were the $\hbar\Omega_{\rm Rabi}$ values, whereas other parameters were used as determined by ARPL. The white dashed-dotted lines and red dashed lines in Fig. 2(c) represent the calculated dispersions of photonic tri-WGMs and polaritonic tri-WGMs, respectively. The results are clear evidence of the strong-coupling regime for our structure with $\hbar\Omega_{\rm Rabi}$ values of 120 ± 7 meV and 117 ± 10 meV for TE and TM, respectively. The value of the Rabi splitting energy is similar to other reported WG polaritons [38] for a single GaN wire system (115 ± 10 meV). This large $\hbar\Omega_{\rm Rabi}$ value, which is

six times larger compared to those of conventional planar cavities [35], is induced by the large spatial overlap between X and CP.

To explore the polariton condensate, we investigated the behavior of the integrated-emission intensity as a function of the pump power (P) for the lower-polariton with mode number 35 (LP35) branch, which only shows nonlinearity, as seen in Fig. 2(d) (bottom). Nonlinearity in the emission was clearly observed at a power density of 1.5 W/cm² (pulse energy ∼150 μJ/cm²), the first threshold power ($P_{\rm th}$), due to the stimulated polariton–polariton scattering. Here, the measured nonlinearity was not photonic lasing but polariton condensate, since the calculated maximum carrier density ($\sim 1 \times 10^{17}$ cm⁻³) at the threshold was 2 orders of magnitude smaller than the X Mott density ($\sim 1 \times 10^{19}$ cm⁻³) of GaN [39]. The nonlinearity of the emission led to the linewidth narrowing of the emission from 8 to 1.19 meV. After the linewidth minimum, linewidth broadening occurred up to 4 meV. Furthermore, a clear blueshift of the peak (8 meV) was observed because of the repulsive interactions of the polariton–polariton and polariton–exciton reservoir, as shown in Fig. 2(d) (top). Additionally, with a further increase in the power density over 5.8 W/cm² (pulse energy ∼580 μJ/cm²) corresponding to the second threshold power ($P_{\rm th2}$), a new peak appeared at a higher energy with a narrower linewidth compared to the polariton condensate, indicating the process of the transition to the weak-coupling regime, as shown in Fig. 2(e) (see Supplement 1). Polaritons can reach the single-mode state due to large mode spacing caused by a small cavity size
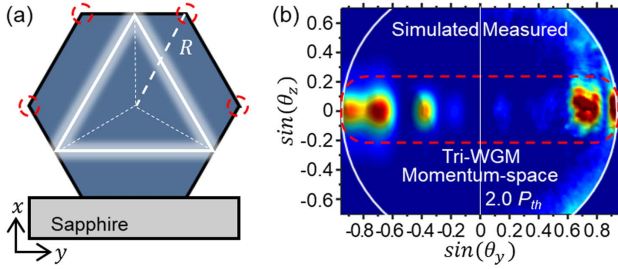
Fig. 3. Identification of photonic mode by the multiple-slit interference methods. (a) Schematics of the cross section of the tri-WGM. Four red circles indicate strong leakage points. (b) FDTD simulated data (left) and measured data (right) at 2.0 P_{th}. The red box represents the interference pattern of the tri-WGM in momentum space.

and relax down to the ground state through strong scattering mediated by a large $\hbar\Omega_{Rabi}$. This large $\hbar\Omega_{Rabi}$ can produce gradual dispersion with a large excitonic fraction, which leads to efficient scattering of polaritons with acoustic phonons [40], compared to the same energy of the ground state with a small $\hbar\Omega_{Rabi}$ and more negatively detuned polariton branch (see Supplement 1). Moreover, a large $\hbar\Omega_{Rabi}$ can help to decouple with a longitudinal optical phonon bath [41], so it can have a large X fraction [42] for enhanced polariton–polariton scattering.

To identify the photonic mode, the momentum space image was measured for observation of the interference pattern [43] generated by each corner of the hexagonal cross section, as shown in Fig. 3(a). Figure 3(b) shows the measured data at 2.0 P_{th} (right) and the simulated data by the FDTD method (left) in momentum-space. The peculiar interference pattern along θ_y is attributed to the multiple-slit interference of the single-mode tri-WG polariton condensate (see Supplement 1), which yields the spatial coherence. This leakage, which is from the four corners [four red circles in Fig. 3(a)] due to the strong scattering, is analogous to the point-like sources going through the slits. The result of the measured data is in excellent agreement with the simulated data, which is the tri-WGM. Thus, we can confidently identify the photonic mode generated in the hexagonal cavity on the substrate. As a result, a room-temperature tri-WG polariton condensate with a single mode is clearly observed on the one-dimensional polariton condensate based on III-nitride semiconductors.

5. TAILORING THE POTENTIAL LANDSCAPE

To explore the low disorder of the wire structure and manipulate the potential landscape, we illuminated two different beam sizes (σ) for the same wire (see Supplement 1). Figures 4(a) and 4(b) represent panchromatic real-space images of the wire for $\sigma = 2000$ nm at 0.05 P_{th} and $\sigma = 200$ nm at 0.07 P_{th}, respectively. Figures 4(c)–4(e) represent the results of ARPL along θ_z for $\sigma = 2000$ nm. The momentum and energy distribution of the polaritons are spread out as shown in Fig. 4(c). With increasing P over P_{th}, the momentum distribution shrank and the emission mostly came from the ground energy state ($\theta_z \sim 0$), as indicated by circle S [Figs. 4(d) and 4(e)]. Polariton condensate was observed only for TM with a linear polarizability of 92% (see Supplement 1). Figures 4(f)–4(h) show the ARPL results for $\sigma = 200$ nm. Interestingly, the momentum distribution was concentrated at a certain angle of the lower polariton branch
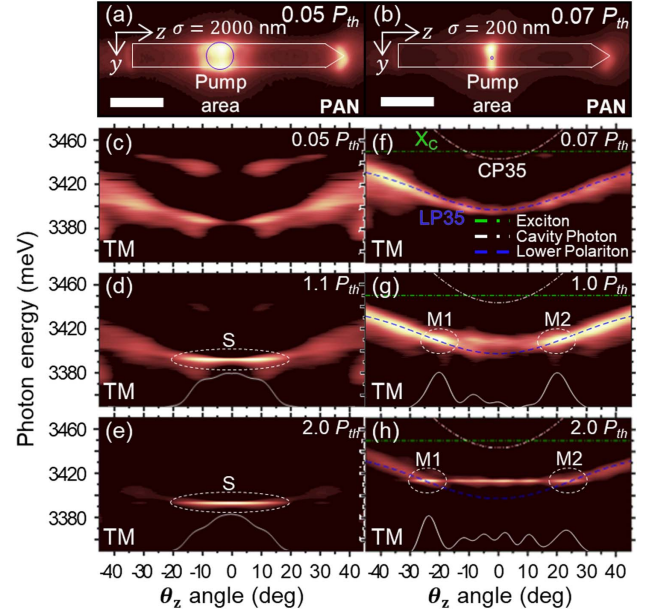

Fig. 4. ARPL via optical manipulation of the potential landscape. (a), (b) Panchromatic image by excitation with a diameter of (a) 2000 nm and (b) 200 nm on the same wire. The scale bars indicate 4 μm. (c)–(e) Power-dependent ARPL via excitation with a diameter of 2000 nm for TM. Note the appearance of polaritonic condensate at zero degrees in dashed circle S. (f)–(h) Power-dependent angle-resolved PL via excitation with a diameter of 200 nm for TM. Note the appearance of extended polaritonic condensate in circle M1 and M2 on the polariton branch.

(red dashed-dotted line) at $P = P_{th}$, as indicated by circles M1 and M2 [Figs. 4(g) and 4(h)]. Here, the polariton condensate obtains a finite momentum on the polariton branch due to the abrupt gradient of the exciton reservoir. The emission at $\theta_z \sim 0$ in the momentum space, corresponding to the pump area in the real space, exhibits very blueshifted energy due to the repulsive interaction with the exciton reservoir generated by the pump area. The nanofocused laser beam ($\sigma = 200$ nm) generates an exciton reservoir with an abrupt landscape in real space, which supplies polaritons to the condensate and also creates a Gaussian-shaped potential landscape for polaritons in real space due to the repulsive interactions between the polariton and the exciton reservoir. Polariton condensate initially occurs at the apex of this tailored potential peak, and the potential energy is transformed to kinetic energy due to the abrupt landscape of the exciton reservoir, so that the polariton condensate obtains a finite momentum [14,17]. This extended polariton condensate has never been explored in conventional III-nitride two-dimensional microcavity systems (to our knowledge) due to the unintentional lateral localization caused by the disorder.

6. CORRELATION BETWEEN MOMENTUM AND REAL SPACE

To explore the one-dimensional ballistic propagation of the polariton condensate, we characterized the space-resolved photoluminescence (SRPL). Figure 5(a) (top) shows a panchromatic real-space image of the wire at $P = 3.0P_{th}$. The main leakage of the tri-WGMs comes from each corner of the hexagonal cavity. Here, the polariton energy increases along the z axis, since the
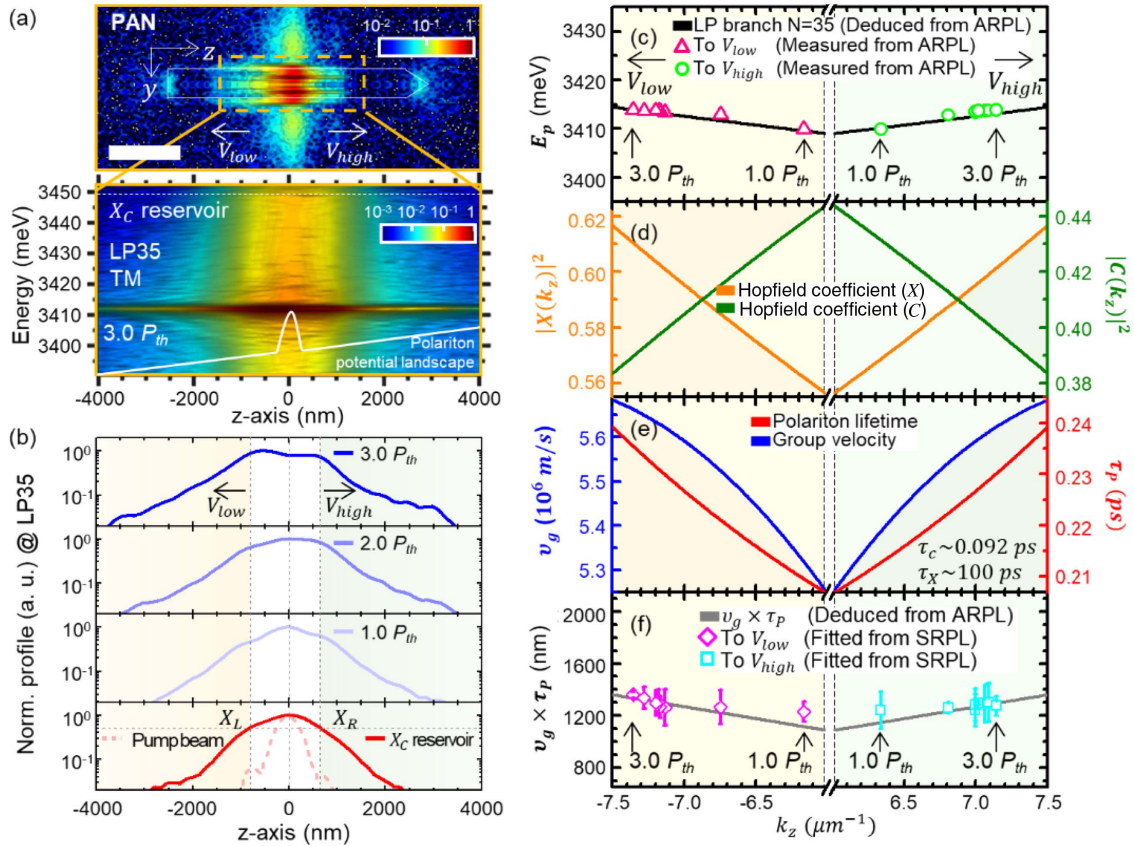
Fig. 5. Manipulation of finite momentum for an extended polariton condensate. (a) Panchromatic image of the same wire at 3.0 P_{th} on a log scale (top). Scale bar indicates 4 μm. Spectrally and spatially resolved emission at 3.0 P_{th} on a log scale (bottom). (b) The spatial profile of laser, X_C, and extended polariton condensate in relation to pump power. Left and right sides are toward V_{low} and V_{high}, respectively. (c) Polariton energy in relation to polariton momentum. The solid line shows calculated dispersion, and the colored triangles and circles show experiment data extracted from ARPL. (d) Corresponding Hopfield coefficient for exciton fraction (orange) and photon fraction (green) from the calculated dispersion, (e) polariton velocity (blue) and polariton lifetime (red) deduced by the LP35 branch, (f) solid line shoes $v_g \times \tau_p$ deduced from ARPL, and colored diamonds and squares show fitted data extracted from SRPL by the tail fitting of far outside approximation.

radius of the top parts of the wire is smaller and the consequent CP photon energy becomes higher than those of the bottom parts. Therefore, with respect to the pump area, the left and right sides are called the downhill potential (V_{low}) and uphill potential (V_{high}), respectively. The results of the SRPL [Fig. 5(a), bottom] show the polariton condensate with quasi-monochromatic energy spread along the z axis due to the finite momentum induced by the potential landscape [12]. We extracted the profiles of the extended polariton condensate along the z axis in relation to P, as shown in Fig. 5(b). The graphs in the bottom part represent the profiles of the pump and exciton reservoirs at 3450 meV. As P increases, two distinct peaks appear on the left and right sides due to the stronger repulsive interaction than in the lower P case.

To characterize the correlation between polaritons in momentum space and real space, we extracted the peak energy (E_p) and wave vector (k_z) from the ARPL in relation to P, as indicated by the colored triangles (left) and circles (right) in Fig. 5(c). As P increases, E_p and consequent k_z increase, completely complying with the calculated LP35 branch [solid line in Fig. 5(c)]. To understand the relative mixing fraction between the exciton ($|X(k_z)|$) and photon ($|C(k_z)|$) of the tri-WG polaritons, we calculated the Hopfield coefficients of the LP35 branch, as shown in Fig. 5(d). As $|k_z|$ increases, the values of $|X(k_z)|$ and $|C(k_z)|$

increase and decrease, respectively. Here, $|X(k_z)|$ and $|C(k_z)|$ are affected by k_z due to the variation of the CP energy. The group velocity of the extended polariton condensate is deduced by $v_g = (1/\hbar)\partial E_p / \partial k_z$, as shown in Fig. 5(e) (left axis). The polariton lifetime (τ_p) is defined as a mixed fraction of the CP lifetime (τ_c) and X lifetime (τ_x), which is $\tau_p^{-1}(k_z) = |C(k_z)|^2/\tau_c + |X(k_z)|^2/\tau_x$. Here, τ_c is determined from the lowest-energy LP branch (~97% photonic-like branch; see Supplement 1) by Fourier transform. The value of τ_c is 0.092 ps (Q factor ~450) for LP33. Here, τ_c is negligibly changed on the mode number and wave vector, so we consider it as a constant. τ_x (100 ps) is the X lifetime measured at room temperature. Consequently, the value of τ_p is shown in Fig. 5(e) (right axis). Here, τ_p can be tailored via the X fraction in the variable of k_z, which is directly controlled by P and σ.

Finally, Fig. 5(f) shows the deduced results of $v_g \times \tau_p$ based on ARPL data [Figs. 4(f)–4(h)] as a solid line as a function of k_z. To define $v_g \times \tau_p$ based on the results of SRPL, we apply the region far outside the pump area [31] for analytical estimation. In this region, polaritons are negligibly influenced by the repulsive potential of the exciton reservoirs and polariton–polariton interaction due to spatial separation from the pump area and the low density of the polaritons, respectively. Considering the tapered

geometry of our structure and the region, the Gross–Pitaevskii equation can be reduced to a one-dimensional Airy equation (see Method B in Section 2) with enhanced directionality due to reduced dimensionality. We carried out tail fittings for spatial profiles as shown in Fig. 5(b) (see Supplement 1). The fitted results of $v_g \times \tau_p$ based on the results of SRPL are represented in Fig. 5(f) by the colored diamonds (left) and squares (right). Here, the fitted results of $v_g \times \tau_p$ based on the SRPL data show excellent agreement with the results of $v_g \times \tau_p$ deduced from the ARPL data without any consideration of the disorder term. This excellent agreement between characterizations of real space and momentum space indicates strong evidence of ballistic propagation, which is the polariton transport with negligible scattering caused by the disorder, due to the ultralow-disorder one-dimensional property of selectively grown wire structures. This ballistic propagation with macroscopic quantum coherence has been observed in the quasi-wire [12] and planar structure [13] based on a GaAs DBR structure at cryogenic temperature. Also, the spatiotemporal evolution of this ballistic propagation of multimode condensate [18] is recently observed in a ZnO wire structure at room temperature. A DBR-based ZnO polariton [44] can obtain ballistic propagation at room temperature, but there is no consistency between real space and momentum space. We focused on this excellent correlation between real space and momentum space for the ballistic propagation of single-mode condensate from the selectively grown GaN wire structure. Furthermore, we can manipulate v_g and τ_p due to the unique features of the polariton system, which exhibits finite momentum and energy within the polariton branch depending on the pump power. Consequently, we can actively control the ballistic propagation of one-dimensional polariton condensate at room temperature. Our proposed platform, a single GaN wire on a substrate having ultralow disorder, opens up the avenue for room-temperature macroscopic quantum coherence with robustness in real one-dimensional structures.

7. CONCLUSION

In this work, we exploit single-mode tri-WG polaritons as an ultralow-disorder system to form and manipulate one-dimensional polariton condensate at room temperature. Selectively grown wires can offer (i) high-quality excitons, (ii) high-quality photons, and (iii) tri-WGMs protecting τ_p from external influences. Non-resonant and nano focused laser illumination induces an abrupt polariton potential gradient via exciton reservoirs, so the polariton condensate acquires finite momentum and energy on the polariton branch. As a result, we can optically manipulate the ballistic propagation of the polariton condensate and consequently bring about the extended polariton condensate being spatially separated from the exciton-reservoir. We anticipate that this ballistic extension will yield a new room-temperature platform for demonstrations of fundamental phenomena analogous to one-dimensional atomic physics. Our platform with wide-bandgap semiconductors offers a breakthrough for nonlinear devices in versatile nanophotonic (polaritonic) applications capable of room-temperature operation.

See Supplement 1 for supporting content.

REFERENCES

1. C. Weisbuch, M. Nishioka, A. Ishikawa, and Y. Arakawa, "Observation of the coupled exciton-photon mode splitting in a semiconductor quantum microcavity," Phys. Rev. Lett. **69**, 3314–3317 (1992).
2. J. Kasprzak, M. Richard, S. Kundermann, A. Baas, P. Jeambrun, J. M. J. Keeling, F. M. Marchetti, M. H. Szymańska, R. André, J. L. Staehli, V. Savona, P. B. Littlewood, B. Deveaud, and L. S. Dang, "Bose–Einstein condensation of exciton polaritons," Nature **443**, 409–414 (2006).
3. R. Balili, V. Hartwell, D. Snoke, L. Pfeiffer, and K. West, "Bose-Einstein condensation of microcavity polaritons in a trap," Science **316**, 1007–1010 (2007).
4. A. Amo, S. Piegeon, C. Adrados, R. Houder, E. Giacobino, C. Ciuti, and A. Bramati, "Light engineering of the polariton landscape in semiconductor microcavities," Phys. Rev. B **82**, 081301 (2010).
5. G. Tosi, G. Christmann, N. G. Berloff, P. Tsotsis, T. Gao, Z. Hatzopoulos, P. G. Savvidis, and J. J. Baumberg, "Sculpting oscillators with light within a nonlinear quantum fluid," Nat. Phys. **8**, 190–194 (2012).
6. E. A. Cerda-Méndez, D. N. Krizhanovskii, M. Wouters, R. Bradley, K. Biermann, K. Guda, R. Hey, P. V. Santos, D. Sarkar, and M. S. Skolnick, "Polariton condensation in dynamic acoustic lattices," Phys. Rev. Lett. **105**, 116402 (2010).
7. A. Amo, T. C. H. Liew, C. Adrados, R. Houdré, E. Giacobino, A. V. Kavokin, and A. Bramati, "Exciton–polariton spin switches," Nat. Photonics **4**, 361–366 (2010).
8. D. Ballarini, M. D. Giorgi, E. Cancellieri, R. Houdré, E. Giacobino, R. Cingolani, A. Bramati, G. Gigli, and D. Sanvitto, "All-optical polariton transistor," Nat. Commun. **4**, 1778 (2013).
9. C. Sturm, D. Tanese, H. S. Nguyen, H. Flayac, E. Galopin, A. Lemaître, I. Sagnes, D. Solnyshkov, A. Amo, G. Malpuech, and J. Bloch, "All-optical phase modulation in a cavity-polariton Mach–Zehnder interferometer," Nat. Commun. **5**, 3278 (2014).
10. H. S. Nguyen, D. Vishnevsky, C. Sturm, D. Tanese, D. Solnyshkov, E. Galopin, A. Lemaître, I. Sagnes, A. Amo, G. Malpuech, and J. Bloch, "Realization of a double-barrier resonant tunneling diode for cavity polaritons," Phys. Rev. Lett. **110**, 236601 (2013).
11. M. Richard, J. Kasprzak, R. Romestain, R. André, and L. S. Dang, "Spontaneous coherent phase transition of polaritons in CdTe microcavities," Phys. Rev. Lett. **94**, 187401 (2005).
12. E. Wertz, L. Ferrier, D. D. Solnyshkov, R. Johne, D. Sanvitto, A. Lemaître, I. Sagnes, R. Grousson, A. V. Kavokin, P. Senellart, G. Malpuech, and J. Bloch, "Spontaneous formation and optical manipulation of extended polariton condensates," Nat. Phys. **6**, 860–864 (2010).
13. B. Nelsen, G. Liu, M. Steger, D. W. Snoke, R. Balili, K. West, and L. Pfeiffer, "Dissipationless flow and sharp threshold of a polariton condensate with long lifetime," Phys. Rev. X **3**, 041015 (2013).
14. D. Ballarini, D. Caputo, C. S. Muñoz, M. D. Giorgi, L. Dominici, M. H. Szymańska, K. West, L. N. Pfeiffer, G. Gigli, F. P. Laussy, and D. Sanvitto, "Macroscopic two-dimensional polariton condensates," Phys. Rev. Lett. **118**, 215301 (2017).
15. D. Caputo, D. Ballarini, G. Dagvadorj, C. S. Muñoz, M. D. Giorgi, L. Dominici, K. West, L. N. Pfeiffer, G. Gigli, F. P. Laussy, M. H. Szymańska, and D. Sanvitto, "Topological order and thermal equilibrium in polariton condensates," Nat. Mater. **17**, 145–151 (2018).
16. D. Sanvitto, S. Pigeon, A. Amo, D. Ballarini, M. D. Giorgi, I. Carusotto, R. Hivet, F. Pisanello, V. G. Sala, P. S. S. Guimaraes, R. Houdré, E. Giacobino, C. Ciuti, A. Bramati, and G. Gigli, "All-optical control of the quantum flow of a polariton condensate," Nat. Photonics **5**, 610–614 (2011).
17. R. Su, J. Wang, J. Zhao, J. Xing, W. Zhao, C. Diederichs, T. C. H. Liew, and Q. Xiong, "Room temperature long-range coherent exciton polariton condensate flow in lead halide perovskites," Sci. Adv. **4**, eaau0244 (2018).

18. T. Michalsky, M. Wille, M. Grundmann, and R. Schmidt-Grund, "Spatiotemporal evolution of coherent polariton modes in ZnO microwire cavities at room temperature," Nano Lett. **18**, 6820–6825 (2018).

19. S. Christopoulos, G. B. H. von Högersthal, A. J. D. Grundy, P. G. Lagoudakis, A. V. Kavokin, J. J. Baumberg, G. Christmann, R. Butté, E. Feltin, J.-F. Carlin, and N. Grandjean, "Room-temperature polariton lasing in semiconductor microcavities," Phys. Rev. Lett. **98**, 126405 (2007).

20. J. Levrat, R. Butté, T. Christian, M. Glauser, E. Feltin, J.-F. Carlin, N. Grandjean, D. Read, A. V. Kavokin, and Y. G. Rubo, "Pinning and depinning of the polarization of exciton-polariton condensates at room temperature," Phys. Rev. Lett. **104**, 166402 (2010).

21. R. Butté, J. Levrat, G. Christmann, E. Feltin, J.-F. Carlin, and N. Grandjean, "Phase diagram of a polariton laser from cryogenic to room temperature," Phys. Rev. B **80**, 233301 (2009).

22. A. Das, J. Heo, M. Jankowski, W. Guo, L. Zhang, H. Deng, and P. Bhattacharya, "Room temperature ultralow threshold GaN nanowire polariton laser," Phys. Rev. Lett. **107**, 066405 (2011).

23. J. Heo, S. Jahangir, B. Xiao, and P. Bhattacharya, "Room-temperature polariton lasing from GaN nanowire array clad by dielectric microcavity," Nano Lett. **13**, 2376–2380 (2013).

24. R. F. Jayaprakash, G. Kalaitzakis, G. Christmann, K. Tsagaraki, M. Hocevar, B. Gayral, E. Monroy, and N. T. Pelekanos, "Ultra-low threshold polariton lasing at room temperature in a GaN membrane microcavity with a zero-dimensional trap," Sci. Rep. **7**, 5542 (2017).

25. R. Tao, K. Kamide, M. Arita, S. Kako, and Y. Arakawa, "Room-temperature observation of trapped exciton-polariton emission in GaN/AlGaN microcavities with air-gap/III-nitride distributed Bragg reflectors," ACS Photon. **3**, 1182–1187 (2016).

26. R. Jedicke, D. Nesvorny, R. Whiteley, Z. Z. Ivezic, and M. Juric, "An age–colour relationship for main-belt S-complex asteroids," Nature **429**, 275–277 (2004).

27. T. Kinoshita, T. Wenger, and D. S. Weiss, "Observation of a one-dimensional Tonks-Girardeau gas," Science **305**, 1125–1128 (2004).

28. L. A. Jauregui, M. T. Pettes, L. P. Rokhinson, L. Shi, and Y. P. Chen, "Magnetic field-induced helical mode and topological transitions in a topological insulator nanoribbon," Nat. Nanotechnol. **11**, 345–351 (2016).

29. S.-Y. Bae, B. O. Jung, K. Lekhal, S. Y. Kim, J. Y. Lee, D.-S. Lee, Y. Honda, and H. Amano, "Highly elongated vertical GaN nanorod arrays on Si substrates with an AlN seed layer by pulsed-mode metal-organic vapor deposition," CrystEngComm **18**, 1505–1514 (2016).

30. D. Zubia and S. D. Hersee, "Nanoheteroepitaxy: the application of nanostructuring and substrate compliance to the heteroepitaxy of mismatched semiconductor materials," J. Appl. Phys. **85**, 6492–6496 (1999).

31. M. Wouters, I. Carusotto, and C. Ciuti, "Spatial and spectral shape of inhomogeneous nonequilibrium exciton-polariton condensates," Phys. Rev. B **77**, 115340 (2008).

32. A. P. Foster, J. P. Bradley, K. Gardner, A. B. Krysa, B. Royall, M. S. Skolnick, and L. R. Wilson, "Linearly polarized emission from an embedded quantum dot using nanowire morphology control," Nano Lett. **15**, 1559–1563 (2015).

33. D. Zhao, C. Zhang, X. Zhang, L. Cai, X. Zhang, P. Luan, Q. Zhang, M. Tu, Y. Wang, W. Zhou, Z. Li, and S. Xie, "Substrate-induced effects on the optical properties of individual ZnO nanorods with different diameters," Nanoscale **6**, 483–491 (2014).

34. M. Kaliteevski, S. Brand, R. Abram, A. Kavokin, and L. S. Dang, "Whispering gallery polaritons in cylindrical cavities," Phys. Rev. B **75**, 233309 (2007).

35. T. Guillet and C. Brimont, "Polariton condensates at room temperature," C. R. Physique **17**, 946–956 (2016).

36. J. Levrat, R. Butté, E. Feltin, J.-F. Carlin, N. Grandjean, D. Solnyshkov, and G. Malpuech, "Condensation phase diagram of cavity polaritons in GaN-based microcavities: experiment and theory," Phys. Rev. B **81**, 125305 (2010).

37. S.-H. Gong, S.-M. Ko, M.-H. Jang, and Y.-H. Cho, "Giant Rabi splitting of whispering gallery polaritons in GaN/InGaN core-shell wire," Nano Lett. **15**, 4517–4524 (2015).

38. A. Trichet, F. Médard, J. Zuniga-Perez, B. Alloing, and M. Richard, "From strong to weak coupling regime in a single GaN microwire up to room temperature," New J. Phys. **14**, 073004 (2012).

39. F. Binet, J. Duboz, J. Off, and F. Scholz, "High-excitation photoluminescence in GaN: hot-carrier effects and the Mott transition," Phys. Rev. B **60**, 4715–4722 (1999).

40. R. Johne, D. Solnyshkov, and G. Malpuech, "Theory of exciton-polariton lasing at room temperature in ZnO microcavities," Appl. Phys. Lett. **93**, 211105 (2008).

41. A. Trichet, L. Sun, G. Pavlovic, N. A. Gippius, G. Malpuech, W. Xie, Z. Chen, M. Richard, and L. S. Dang, "One-dimensional ZnO exciton polaritons with negligible thermal broadening at room temperature," Phys. Rev. B **83**, 041302 (2011).

42. F. Li, L. Orosz, O. Kamoun, S. Bouchoule, C. Brimont, P. Disseix, T. Guillet, X. Lafosse, M. Leroux, J. Leymarie, M. Mexis, M. Mihailovic, G. Patriarche, F. Réveret, D. Solnyshkov, J. Zuniga-Perez, and G. Malpuech, "From excitonic to photonic polariton condensate in a ZnO-based microcavity," Phys. Rev. Lett. **110**, 196406 (2013).

43. D. Saxena, F. Wang, Q. Gao, S. Mokkapati, H. H. Tan, and C. Jagadish, "Mode profiling of semiconductor nanowire lasers," Nano Lett. **15**, 5342–5348 (2015).

44. R. Hahe, C. Brimont, P. Valvin, T. Guillet, F. Li, M. Leroux, J. Zuniga-Perez, X. Lafosse, G. Patriarche, and S. Bouchoule, "Interplay between tightly focused excitation and ballistic propagation of polariton condensates in a ZnO microcavity," Phys. Rev. B **92**, 235308 (2015).